Contrib Mineral Petrol (2010) 159:25–42
DOI 10.1007/s00410-009-0414-5

ORIGINAL PAPER

An experimental investigation of antigorite dehydration in natural silica-enriched serpentinite

José Alberto Padrón-Navarta · Jörg Hermann · Carlos J. Garrido · Vicente López Sánchez-Vizcaíno · María Teresa Gómez-Pugnaire

Received: 13 February 2009 / Accepted: 29 May 2009 / Published online: 20 June 2009

Abstract Piston cylinder experiments were performed to constrain the pressure and temperature conditions for two high-pressure antigorite dehydration reactions found in silica-enriched serpentinites from Cerro del Almirez (Nevado–Filábride Complex, Betic Cordillera, southern Spain). At 630–660°C and pressures greater than 1.6 GPa, antigorite first reacts with talc to form orthopyroxene ± chlorite + fluid. We show that orthopyroxene + antigorite is restricted to high-pressure metamorphism of silica-enriched serpentinite. This uncommon assemblage is helpful in constraining metamorphic conditions in cold subduction environments, where antigorite serpentinites have no diagnostic assemblages over a large pressure and temperature range. The second dehydration reaction leads to the breakdown of antigorite to olivine + orthopyroxene + chlorite + fluid. The maximum stability of antigorite is found at 680°C at 1.9 GPa, which also corresponds to the maximum pressure limit for tremolite coexisting with olivine + orthopyroxene. The high aluminium (3.70 wt% Al_2O_3) and chromium contents (0.59 wt% Cr_2O_3) of antigorite in the investigated starting material is responsible for the expansion of the serpentinite stability to 60–70°C higher temperatures at 1.8 GPa than the antigorite stability calculated in the Al-free system. The antigorite from our study has the highest Al–Cr contents among all experimental studies and therefore likely constraints the maximum stability of antigorite in natural systems. Comparison of experimental results with olivine–orthopyroxene–chlorite–tremolite assemblages outcropping in Cerro del Almirez indicates that peak metamorphic conditions were 680–710°C and 1.6–1.9 GPa.

Keywords Antigorite dehydration · Silica metasomatism · Orthopyroxene-bearing serpentinite

Communicated by J. Hoefs.

Electronic supplementary material The online version of this article (doi:10.1007/s00410-009-0414-5) contains supplementary material, which is available to authorized users.

J. A. Padrón-Navarta (✉)
Departamento de Mineralogía y Petrología,
Facultad de Ciencias, Universidad de Granada,
Avda Fuentenueva s/n, 18002 Granada, Spain
e-mail: padron@ugr.es

J. Hermann
Research School of Earth Sciences,
The Australian National University,
Canberra 0200, ACT, Australia

C. J. Garrido
Instituto Andaluz de Ciencias de la Tierra (IACT),
CSIC & UGR, 18002 Granada, Spain

V. López Sánchez-Vizcaíno
Departamento de Geología, Escuela Politécnica Superior,
Universidad de Jaén, Alfonso X El Sabio 28,
23700 Linares, Spain

M. T. Gómez-Pugnaire
Departamento de Mineralogía y Petrología,
Facultad de Ciencias, Instituto Andaluz de Ciencias de la Tierra,
Universidad de Granada - CSIC, 18002 Granada, Spain

Introduction

Pioneering experimental work on the pressure-temperature stability of a serpentine mineral, antigorite, demonstrated the potential role of ultramafic rocks as H_2O-carrier to a depth of ≤200 km in subduction zones (for a comprehensive review see Ulmer and Trommsdorff 1999). The hydration of the upper mantle extensively occurs when

oceanic lithosphere undergoes seafloor hydrothermal alteration at mid-ocean ridges (O'Hanley 1996; Bach et al. 2004, 2006), during submarine exhumation of subcontinental mantle rocks (Boillot et al. 1989; Lagabrielle and Bodinier 2008), during bending-related faulting of the slab across the ocean trench (Peacock 2001; Ranero et al. 2003) and when fluids released from the dehydration of the downgoing slab interact with cold parts of the mantle wedge (Tatsumi 1989; Bebout and Barton 1989; Guillot et al. 2000, 2001; Fumagalli and Poli 2005). A major area of interest is the link between the antigorite dehydration and the generation of arc volcanism (Tatsumi 1989; Ulmer and Trommsdorff 1995; Schmidt and Poli 1998). Observed *P*-wave velocities in active subduction zones and numerical modeling let Iwamori and Zhao (2000) to suggest that most of the H_2O released from the dehydration of the oceanic crust is incorporated back into the mantle wedge forming relatively thin (<7 km) "serpentinite channels" along the top surface of the subducting slab. More recently, the existence of these channels of hydrated mantle material has been suggested by detailed reflectivity profiles beneath northeastern Japan (Kawakatsu and Watada 2007).

An exceptional locality to survey the high-pressure antigorite dehydration is the Cerro del Almirez ultramafic massif (Nevado–Filábride Complex, Betic Cordillera, southern Spain) (Trommsdorff et al. 1998; Puga et al. 1999; López Sánchez-Vizcaíno et al. 2005, 2009; Garrido et al. 2005). The antigorite breakdown took place during the Alpine collision in the Middle Miocene (López Sánchez-Vizcaíno et al. 2001) when serpentinites (antigorite + magnetite + olivine + tremolite/diopside) were subducted to depths of up to 70 km forming prograde chlorite harzburgite (olivine + orthopyroxene + chlorite + tremolite + magnetite) with spinifex-like textured olivine and orthopyroxene (Trommsdorff et al. 1998). This ultramafic massif has been used as a natural laboratory to investigate the composition of fluids during the high-P dehydration of serpentinites and the origin of the depletion of high-field-strength trace elements in subduction zone fluids (Scambelluri et al. 2001, 2004a, 2004b, 2007; Garrido et al. 2005). Close to the antigorite-out isograd metre-scale lenses occur consisting of antigorite + orthopyroxene + tremolite + magnetite ± olivine, referred to here as antigorite–orthopyroxene assemblage or simply orthopyroxene-bearing serpentinite. This unusual paragenesis could originate from an additional antigorite dehydration reaction in a Si-enriched serpentinite (Spandler et al. 2008).

Previous experimental studies have demonstrated that the content of aluminium and chromium and the extent of polysomatic ordering have a great influence on the stability of antigorite (Bromiley and Pawley 2003; Wunder et al. 2001). Antigorite from Cerro del Almirez is highly ordered and has high iron, aluminium and chromium contents (Trommsdorff et al. 1998; Padrón-Navarta et al. 2008). Therefore, these samples represent a perfect starting material to experimentally investigate the stability of antigorite in natural systems in a subduction environment. In this paper we present an experimental approach to constrain the full grid in the natural $CaO–FeO–MgO–Al_2O_3–SiO_2–H_2O$ system (CFMASH) for a hydrated ultramafic composition using a Si-enriched (orthopyroxene-bearing) serpentinite from Cerro del Almirez. The experimental results are compared to a calculated pseudosection for the same composition. This information is used to constrain the maximum thermal stability of antigorite at high-P in this ultramafic massif and to investigate the significance of the antigorite–orthopyroxene assemblage in subduction zones.

Background and experimental strategy

Under water-saturated conditions and bulk compositions between antigorite and olivine (e.g. as the average of Cerro del Almirez serpentinite, bulk-1 in Fig. 1, Garrido et al. 2005) antigorite dehydrates above the invariant point [Di] (invariant points are labelled with the absent phase in brackets) exclusively through the reaction (see Fig. 2a for the loci of reactions, mineral abbreviations are given in Fig. 1):

$$\text{Atg} \leftrightarrow \text{Ol} + \text{Opx} + \text{L} \quad (1)$$

However, in silica enriched bulk composition (Si-enriched bulk serpentinite composition is defined here as Si/Mg molar ratio higher than in the antigorite and lower than in the talc, i.e. 4/3 > Si/Mg > 34/48, e.g. bulk-2 and bulk-3 in Figs. 1, 2c) antigorite reacts with talc through the reaction (Fig. 2a):

$$\text{Atg} + \text{Tlc} \leftrightarrow \text{Opx} + \text{L} \quad (2)$$

At lower pressures (i.e. below the invariant point [Di]) antigorite dehydrates in both bulk compositions through reaction (3):

$$\text{Atg} \leftrightarrow \text{Ol} + \text{Tlc} + \text{L} \quad (3)$$

While there is a number of field evidence for the occurrence of reaction (3) in contact metamorphism of hydrated ultramafic rocks (Trommsdorff and Evans 1972, 1974; Springer 1974; Frost 1975; Arai 1975; Irving and Ashley 1976; Pinsent and Hirst 1977; Vance and Dungan 1977; Matthes and Knauer 1981; Worden et al. 1991; Nozaka and Shibata 1995), the occurrence of reaction (1) in natural rocks has been only reported in Cerro del Almirez (Trommsdorff et al. 1998). Reaction (2) is expected to be even more restricted in nature, as it requires a more specific serpentinite bulk composition.

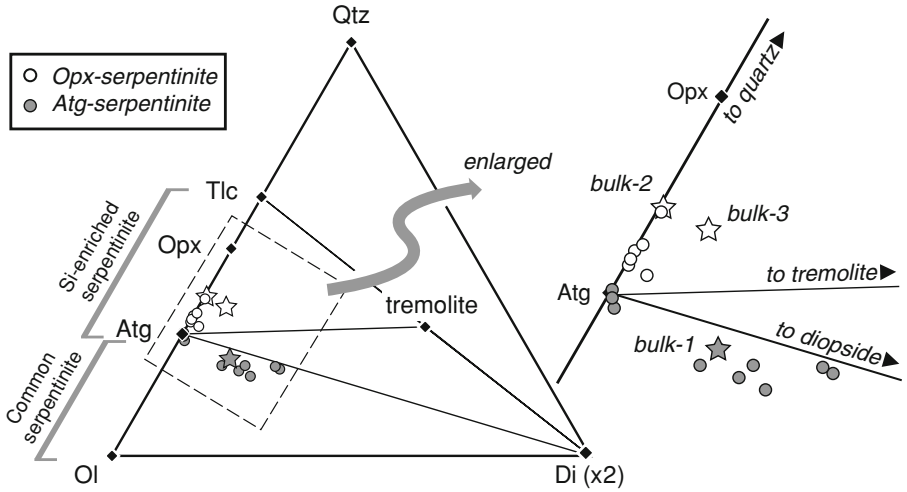

Fig. 1 Definition of the terms "common serpentinite" (on the tie-line between olivine and antigorite, $1/2 < Si/Mg < 34/48$, in molar proportion) and "Si-enriched serpentinite" (on the tie-line between the antigorite and talc, $34/48 < Si/Mg < 4/3$) in the quartz–forsterite–diopside ternary diagram projected from H_2O. Compositions of the two types of serpentinite observed in Cerro del Almirez (antigorite–serpentinite and orthopyroxene-bearing serpentinite) plot in two different three-phase *triangles*. Bulk-1 to bulk-3 are different bulk compositions discussed in the text (see Tables 1, 2). Mineral abbreviations: *Tlc* talc, *Opx* orthopyroxene, *Atg* antigorite, *Ol* olivine, *Di* diopside, *Tr* tremolite, *Qtz* quartz. Other mineral abbreviations used in the text: *Chl* chlorite, *L* liquid phase, *Mgt* magnetite, *Pn* pentlandite. Diagram generated using the program CSpace, Torres-Roldán et al. 2000

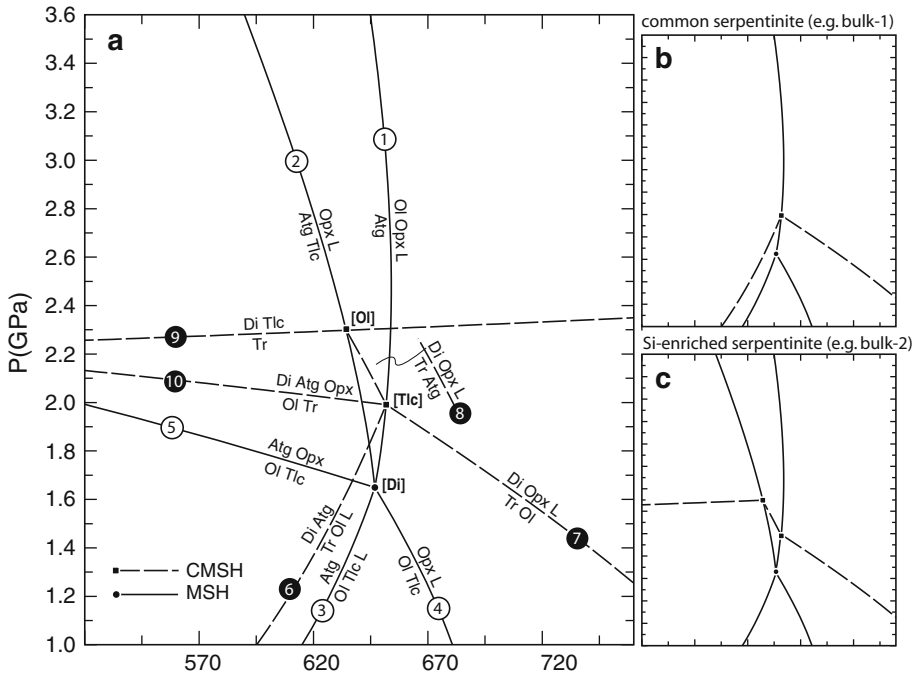

Fig. 2 **a** Phase relations relative to hydrated mantle rocks in the simplified system $CaO–MgO–SiO_2–H_2O$ (*CMSH*) computed with PerpleX package (Connolly 2005) and the updated Holland and Powell's (1998) database (hp02ver.dat) with reactions labelled like in the text. The CORK equation of state from Holland and Powell (1998) for H_2O (labelled as L) was chosen. The invariant points [Di], [Tlc] and [Ol] are labelled with the absent phase. See Fig. 1 for mineral abbreviation. **b** Relevant reactions for a water-saturated common serpentinite (bulk-1) and **c** for a water saturated Si-enriched serpentinite (bulk-2 and bulk-3)

When calcium is considered in the system, diopside and tremolite appear as two separated phases involved in five reactions (6, 7, 8, 9, 10, where reaction (9) is degenerated (Fig. 2a). The appearance of tremolite through reaction (6) occurs typically in normal serpentinite with increasing grade (e.g. Trommsdorff and Evans 1972). In contrast, for a Si-enriched composition tremolite is not a diagnostic mineral because its stability field expands to lower temperature and higher pressure. In such a bulk composition the stability field of coexisting tremolite-antigorite is delimited by reactions (8) and (9) (Fig. 2c). Beyond the antigorite stability field, tremolite breaks down through reaction (7) for both bulk compositions, defining the boundary between the amphibolite facies and the granulite facies in ultramafic rocks (Evans 1977).

In contrast to calcium, iron can substitute for magnesium in all silicates considered above. So the addition of iron only increases the thermodynamic variance of the

system without adding any new phase or new reactions. Moreover, the addition of iron to the system displaces all the reactions to lower temperatures (Worden et al. 1991; Bromiley and Pawley 2003). The addition of Al also increases the variance of reactions involving antigorite because it can be incorporated in it through tschermaks exchange. As tschermaks exchange is limited in the orthopyroxene at the temperature considered here and does not exist in the olivine, chlorite appears in the products from the antigorite dehydration reactions (1) (Bromiley and Pawley 2003) and (3) (Worden et al. 1991) and, although it has not yet been described, it is expected to occur also in reaction (2).

In this work we use a phase diagram approach in order to establish a more complete grid for natural serpentinite than previously reported. In this approach, the reactions are constrained by comparing runs with contrasting mineral assemblages. In natural systems a full reversal experimental approach is difficult to interpret as the reactions are not truly univariant. Although the relatively low temperature runs used in the experiments prevents the attainment of complete equilibrium, this approach has been found successful when reproducing the expected sequence of reactions with increasing temperature. A larger number of reactions can be determined using a Si-enriched composition instead of using a common serpentinite composition (Fig. 2b, c). Thus, a natural Si-enriched bulk composition from the Cerro del Almirez locality was selected with the aim of constraining reactions (1) and (2). The assemblage of the selected starting material is composed of five (Opx + Atg + Tr + Tlc + Ol) solid phases and contains minerals of both the reactant and product sides of the investigated reactions. This enables us to use the starting material in a quasi-reversal experimental approach where the new growth of stable phases and the disappearance of unstable phases can be monitored.

Starting material

Most of the antigorite serpentinites outcropping in the Cerro del Almirez are quite homogeneous in composition (Trommsdorff et al. 1998; López Sánchez-Vizcaíno et al. 2005; Garrido et al. 2005) except for CaO. The extent of CaO variation in the bulk composition is directly related with the heterogeneous distribution of relic clinopyroxene in the protolith (Fig. 1, bulk-1). Antigorite from Cerro del Almirez is exceptionally ordered and consists of the polysome $m = 17$ (Padrón-Navarta et al. 2008), where m is the number of tetrahedra in a single chain defined by the antigorite wavelength. This high polysomatic ordering is distinctive of well-equilibrated antigorite in high-grade terrains (Mellini et al. 1987; Capitani and Mellini 2004).

Sample Al06-37 (bulk-2) is an antigorite serpentinite with centimetre-sized orthopyroxene porphyroblasts partially or completely replaced by retrograde talc (Fig. 3). Orthopyroxene is commonly elongated with aspect ratios (length/with ratio) of 2.75 ± 0.55. This sample has a remarkably higher silica (Fig. 1, bulk-2) content with respect to other Almirez serpentinites (Fig. 1, bulk-1). To our knowledge, this is the first report of high-pressure orthopyroxene-bearing serpentinite. Antigorite from sample Al06-37 has high aluminium (3.70 ± 0.34 wt% Al_2O_3; Table 1) and chromium contents (0.59 ± 0.08 wt% Cr_2O_3), and is also highly ordered, polysome ranging from $m = 15$ to $m = 16$ (M. Mellini, personal communication, 2009). Tremolite is scarce and spatially associated with orthopyroxene. Olivine occurs in the matrix (Table 1; Fig. 3) and rarely as centimetre-sized veins cutting the foliation. Magnetite (chromium-magnetite and titaniferous magnetite) and pentlandite are also present as accessory minerals.

Large blocks of Si-enriched serpentinite (six samples, usually >2 kg) were cleaned and cut in parallelepipeds

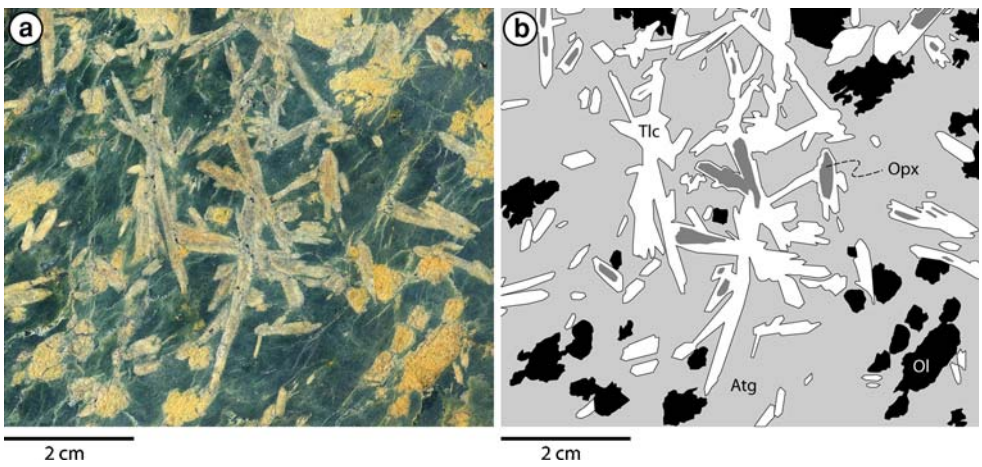

Fig. 3 **a** Representative texture of a Si-enriched serpentinite (scanned polished-surface of sample Al06-37). The hand-sample was cut closely parallel to the rock foliation. **b** Sketch highlighting textural relationships between the elongated talc-pseudomorphs after enstatite (up to 2 cm in length) and olivine in the antigorite matrix. Mineral modes in Table 1 were estimated by image analysis using the whole area of this sketch (c. 8 × 7 cm)

Table 1 Mode and composition (average and 1σ) of the starting material (sample Al06-37, bulk-2)

Weight %	Atg (n = 16)	Opx (n = 43)	Tremolite (n = 10)	Olivine (n = 52)	Talc (n = 38)	Mag (n = 4)		[a]Bulk-1	Bulk-2	Bulk-3
Mode[b]	66.8	3.5	–	9.9	19.8	–				
SiO_2	42.38 (0.61)	58.22 (0.66)	59.14 (0.62)	41.29 (0.40)	62.85 (1.71)	0.16 (0.25)	SiO_2	40.54 (0.69)	45.07	44.90
TiO_2	0.02 (0.01)	0.02 (0.01)	0.02 (0.01)	b.d.l.	0.02 (0.01)	0.29 (0.03)	TiO_2	0.17 (0.21)	0.08	0.08
Al_2O_3	3.70 (0.34)	0.03 (0.06)	0.21 (0.12)	b.d.l.	0.09 (0.06)	0.05 (0.02)	Al_2O_3	2.75 (0.46)	2.19	3.10
Cr_2O_3	0.59 (0.08)	0.02 (0.01)	0.02 (0.01)	b.d.l.	b.d.l.	1.71 (0.35)	Fe_2O_3	8.06 (0.45)	3.08	2.99
$Fe_2O_3^c$						66.05 (1.86)	FeO[d]	–	3.78	3.67
FeO	4.05 (0.16)	8.04 (0.20)	1.87 (0.16)	11.19 (0.52)	1.24 (0.34)	30.62 (0.19)	MgO	36.35 (1.71)	36.98	35.90
NiO	0.09 (0.03)	0.04 (0.01)	0.05 (0.01)	0.26 (0.03)	0.07 (0.02)	0.23 (0.02)	MnO	0.11 (0.02)	0.09	0.09
MgO	38.44 (0.39)	34.82 (0.42)	24.42 (0.40)	49.14 (1.02)	31.41 (1.19)	0.52 (0.11)	CaO	2.45 (1.88)	0.16	1.23
MnO	0.04 (0.01)	0.39 (0.03)	0.12 (0.05)	0.17 (0.04)	b.d.l.	0.06 (0.00)	Na_2O	b.d.l.	0.05	0.05
CaO	0.02 (0.01)	0.12 (0.03)	13.12 (0.29)	0.02 (0.02)	0.05 (0.09)	0.02 (0.00)	L.O.I.	10.07 (1.15)	7.71	8.00
Na_2O	b.d.l.	0.01 (0.02)	0.23 (0.17)	b.d.l.	0.06 (0.05)		Total	100.51 (0.44)	99.19	100.00
H_2O calc	12.25 (0.13)		2.23 (0.02)		4.74 (0.08)					
Total	101.57 (1.78)	101.72 (1.48)	101.42 (1.95)	102.07 (2.15)	100.53 (3.61)	99.72 (2.86)				
Ions calculated on the basis of 4 oxygens (olivine), 6 oxygens (orthopyroxene), 11 oxygens (talc), 23 oxygens and Fe^{3+}/Fe_{tot} = 0 (amphibole), 6.823 oxygens and Fe^{3+}/Fe_{tot} = 0 (antigorite, m=17) and 3 cations (magnetite)										
Si	1.892 (0.016)	1.988 (0.011)	7.948 (0.037)	0.997 (0.010)	3.974 (0.064)	0.006 (0.010)				
Ti	0.001 (0.000)	0.000 (0.000)	0.002 (0.001)		0.001 (0.001)	0.008 (0.001)				
Al	0.194 (0.018)	0.001 (0.002)	0.033 (0.019)		0.007 (0.004)	0.002 (0.001)				
Cr	0.021 (0.003)	0.000 (0.000)	0.002 (0.001)			0.051 (0.010)				
Fe^{3+}						1.918 (0.013)				
Fe^{2+}	0.151 (0.006)	0.230 (0.005)	0.210 (0.018)	0.226 (0.010)	0.065 (0.019)	0.973 (0.005)				
Ni	0.003 (0.001)	0.001 (0.000)	0.005 (0.001)	0.005 (0.001)	0.004 (0.001)	0.007 (0.001)				
Mn	0.002 (0.000)	0.011 (0.001)	0.013 (0.006)	0.004 (0.001)		0.002 (0.000)				
Mg	2.558 (0.013)	1.773 (0.024)	4.894 (0.075)	1.769 (0.027)	2.961 (0.118)	0.029 (0.006)				
Ca	0.001 (0.000)	0.004 (0.001)	1.890 (0.045)		0.003 (0.006)	0.001 (0.000)				
Na			0.059 (0.044)		0.007 (0.006)					
Sum cations	4.823 (0.008)	4.011 (0.011)	15.062 (0.040)	3.003 (0.010)	7.025 (0.064)	3.000				
OH	3.647		2.000		2.000					
X_{Mg}	0.942 (0.002)	0.880 (0.003)	0.955 (0.004)	0.883 (0.008)	0.977 (0.006)	0.029 (0.006)				

[X_{Mg} is Mg atoms/(Mg + Fe + Mn + Ni) atoms] and other bulk compositions described in the text. The detection limit for the XRF analyses is 0.01 wt.% except for L.O.I. 0.05 wt.%

[a] Bulk-1: Almirez serpentinite average (Garrido et al. 2005); bulk-2: Si-enriched serpentinite (sample Al06-37); bulk-3: the same as bulk-2 but with 2.29 wt.% wollastonite and 1.53 wt.% $Al(OH)_3$ added

[b] Calculated using image analyses on the polished surface of hand sample Al06-37 (Fig. 3) neglecting tremolite and magnetite, not visible at this scale

[c] Calculated assuming stoichiometry. *L.O.I*, loss on ignition; *b.d.l.* below detection limit

[d] Ferrous iron was determined by potentiometric analysis in bulk-2 (sample Al06-37). In bulk-1 ferrous iron was not determinated and Fe_{tot} is expresed as Fe_2O_3

(4–6 cm in length) with a diamond saw. Final parallelepipeds (0.5–1 kg) where crushed in a steel jaw crusher and quartered several times in a riffle-splitter. The resulting aliquots were pulverised in an agate ring mill. Whole rock major elements were analysed using standard X-ray fluorescence procedure (XRF) in the Geoscience Laboratories (GeoLabs), Ontario Geological Survey, Sudbury, Canada. The samples were first run for loss on ignition and then fused with borate flux to produce a glass bead. Ferrous iron was determined in the same laboratory by potentiometric analysis using potassium permanganate as oxidation agent. Ferric iron was calculated from the difference of the total iron measured by XRF and the measured ferrous iron. The composition of the sample Al06-37 (bulk-2; Table 1), together with other Si-enriched serpentinite samples, is plotted in Fig. 1.

Except for one exploratory run (C-2967; Table 2), the experiments were performed using a slightly modified

Table 2 Starting material, experimental conditions and assemblages

Label	Notes					Major phases	Minor phases
Bulk-2	Si-enriched serpentinite (sample Al06-37)					Atg, Tr, Tlc, Opx, Ol	Mgt, Pn
Bulk-3	Bulk-2 modified for the experiments					The same as above plus wollastonite and $Al(OH)_3$	
Run no.	Start mat	*P* (kbar)	*T* (°C)	Time (h)	Weight loss (%)[a]	Major phases	Minor phases
C-2990	Bulk-3	16.0	640	168	0.2	Atg, **Tr**, Tlc, *Ol*	Mgt, Pn
C-2989	Bulk-3	16.0	660	168	1.0	Atg, **Tr**, Tlc, *Opx, Ol*	Mgt, Pn
C-3004	Bulk-3	16.0	680	168	7.4	**Tr**, **Opx, Ol, Chl**	Mgt, Pn
C-3044	Bulk-3	18.0	680	168	6.0	Atg, **Tr**, **Opx, Ol, Chl**	Mgt, Pn
C-3012	Bulk-3	18.0	700	168	NA	**Opx, Ol, Chl**, (Di)	Pn
D-912	Bulk-3	20.0	600	168	0.0	Atg, **Tr**, Tlc, *Ol*	Mgt, Pn
C-2978	Bulk-3	20.0	650	168	NA	Atg, **Tr**, Tlc, *Opx, Ol*	Mgt, Pn
C-3003	Bulk-3	20.0	670	168	1.8	Atg, **Tr**, **Opx, Ol, Chl**	Mgt, Pn
C-3011	Bulk-3	20.0	700	168	NA	**Opx, Ol, Chl**, (Di)	Pn
C-3219	Bulk-3	22.5	625	168	1.8	Atg, Tr, Tlc, **Opx,** *Ol*, **Chl**	Pn
C-3220	Bulk-3	22.5	665	168	2.2	Atg, **Opx, Ol, Chl**, (Di)	Pn
D-756	Bulk-3	22.5	680	168	6.5	**Opx, Ol, Chl**, (Di)	Mgt, Pn
C-2967	Bulk-2	25.0	670	120	NA	**Opx, Ol, Chl**	Pn

See Fig. 1 for mineral abbreviations. Cleary growing new phases in bold, not growing and relic phases from the starting material in roman and italics, respectively. (Di) diopside is not in textural nor chemical in equilibrium

NA not available

[a] Loss of weight of the experimental capsule after its piercing and drying in the oven

composition from sample Al06-37 (referred to here as bulk-3; Fig. 1). Fresh pieces of sample Al06-37 (bulk-2) were crushed and ground in an agate mortar under acetone. We added 2.29 wt% of synthetic wollastonite ($CaSiO_3$) and 1.53 wt% of aluminium hydroxide $Al(OH)_3$ to this composition in order to increase the modal amount of tremolite and diopside that could form and slightly increase the Al_2O_3 and H_2O by 1.0 and 0.5 wt%, respectively (bulk-3; Table 1, Fig. 1). The final grain size distribution of the starting material used in the experiments was measured by soft X-ray monitored gravity sedimentation (SediGraph 5100, Micromeritics® at the University of Granada). More than 80% of the starting material was normally distributed below 10 μm (with a mean value ca. 5 μm), and the rest of the population clustered around 12–18 μm. Both bulk compositions (bulk-2 and bulk-3, Fig. 1) plot inside the antigorite–orthopyroxene–tremolite triangle and, thus, both of them result in the same phase relations.

Experimental and analytical techniques

The experiments reported here are conventional quenching experiments conducted in a range of 1.6–2.5 GPa and 600–700°C. Experiments were performed in 0.5-inch (12.7 mm) end-loaded piston cylinder apparatuses at the Research School of Earth Science (The Australian National University) using a vessel with a 32-mm length bore, employing pure NaCl, low friction assemblies. Sample containers were Au-capsules with an outer diameter of 2.3 and 6–7 mm in outer length resulting in cylindrical samples of 4–6 mm in length. Temperature gradients within the capsule depend, among other factors, on the temperature, pressure, capsule material, assembly design, heater shape and type of solid pressure transmitting media (Schilling and Wunder 2004). This complex interrelation of factors and the additionally observed off-centre hotspot effect (Pickering et al. 1998) prevent an accurate determination of the temperature gradient in the actual runs. Watson et al. (2002), however, measured at 1,400°C, a decrease in temperature of 10–25°C, at distances of 2–3 mm from the hotspot using a reaction-progress thermometer. For lower temperatures, as those employed in our experiments, the temperature gradient is expected to be much smaller (Schilling and Wunder 2004), in the range of the thermocouple accuracy. Gold capsules were placed in a MgO tube, inside a Teflon coated NaCl-graphite assembly. The use of gold capsule and the "dry" furnace assembly produces conditions close to the Ni–NiO transition (Hermann and Spandler 2008), which is similar to the FMQ buffer in the investigated temperature range. Capsules were welded shut and tested for leakage prior to the experiment. A disk of 1-mm MgO was placed between the thermocouple end-point and the capsule to avoid reaction between them. Pressure was measured

directly, converting the load in the cell to pressure for a low friction assembly and was kept constant during the experiments. No pressure corrections were applied because of the low friction behaviour of the NaCl cells and the relatively long run durations. Measurements on piston travel have shown that in such an assembly and given run temperatures, friction dissipates within the first 24–36 h. From this we estimate that pressure is accurate within ±0.1 GPa. Temperatures were measured using type B thermocouples ($Pt_{94}Rh_6$–$Pt_{70}Rh_{30}$), protected by two bore mullite tubes. The thermocouple precision is better than ±2°C and accuracy is ±10°C. The samples were quenched at the end of the runs by turning off the power of the furnace. Afterwards the experiments capsules were pinched and dried in the oven for 4 h. They were mounted in epoxy and ground down until a representative section was exposed.

Mineral analyses of the natural sample used as starting material in the experiments (Al06-37) were performed using a Cameca SX100 electron microprobe at the RSES (Australian National University) with operating conditions of 15-kV acceleration voltage, and 20-nA beam current (Table 1). Natural and synthetic mineral and glasses were used as standards. The resulting phases from the experiments were observed in polished mounts under backscattered electron images and analysed using a JEOL JSM 6400 scanning electron microscope (SEM) (Electron Microscopy Unit, ANU), equipped with a LINK-ISIS energy dispersive spectrometer (EDS), operated at 15-kV accelerating voltage, 1-nA beam current and a working distance of 39 mm, with counting time of 100 s. No differences were observed using a spot or defocused beam due to the low alkalis concentration in the hydrous phases (Supplementary Table).

Results

Phase relations

Mineral assemblages at different pressure and temperature conditions are presented in Table 2 and plotted in Fig. 4. The appearance or disappearance curves of key phases were obtained by detailed textural studies of the run assemblages and comparison with the starting material. Lower temperatures runs (D-912, C-2990) show little textural evidences of reaction except for the disappearance of orthopyroxene and growth of tremolite. Olivine grain shapes in these runs are anhedral and sharp indicating they are relicts (Fig. 5a). This suggests that water saturated conditions were not attained and that the water was first consumed to form tremolite and talc + antigorite at the expense of wollastonite and orthopyroxene, respectively, before olivine completely reacted out.

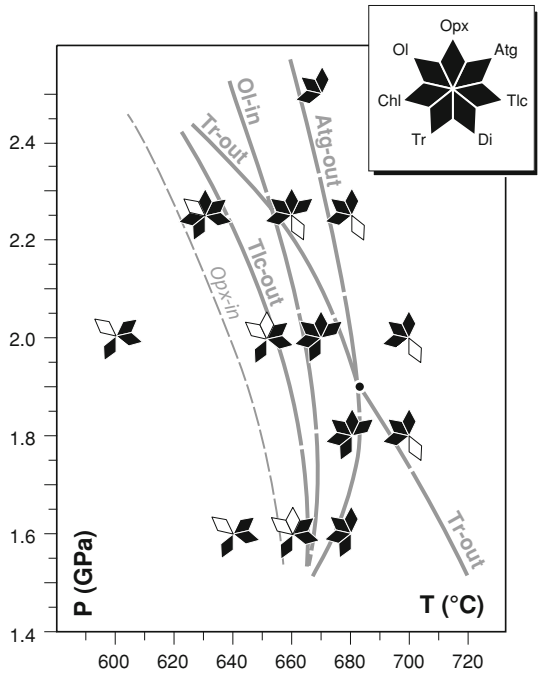

Fig. 4 Experimental results in the P–T space. Phases in textural equilibrium are shown in *black*. *Empty diamonds* indicate relic phases and diopside (always in textural and chemical disequilibrium). Opx-in curve (*dashed line*) is poorly constrained. See Fig. 1 for mineral abbreviations

Opx-in reaction

Minor orthopyroxene observed in runs C-3219, C-2978 and C-2989 is anhedral and, at least in part, is a relict phase from the starting material based on the average grain size (16.0 ± 8.3 μm) and low aspect ratio (1.7 ± 0.5). Nevertheless, no textural evidences of its breakdown were found indicating that either it is in equilibrium with the assemblage or the kinetic barrier of the reaction was not attained. Small amounts of chlorite were detected in one of these runs (C-3219) together with small (2.9 ± 1.4 μm) but euhedral and prismatic orthopyroxene (3.0 ± 1.3 aspect ratio). Because of the high Al-content of the reactant antigorite and the low Al-content of the produced orthopyroxene, we interpret that this chlorite is formed by the reaction between antigorite and talc to produce orthopyroxene [reaction (2)]. This allows us to tentatively trace the Opx-in curve from 650°C at 1.5 GPa to c. 600°C at 2.5 GPa (Fig. 4). More interestingly, talc, occurring as irregular patches in the matrix, is still stable in all these runs (C-3219, C-2978 and C-2989) indicating that Tlc-out and Opx-in curves are not coincident.

Tlc-out and Ol-in reactions

With increasing temperature talc completely disappears and new idiomorphic orthopyroxene and olivine are

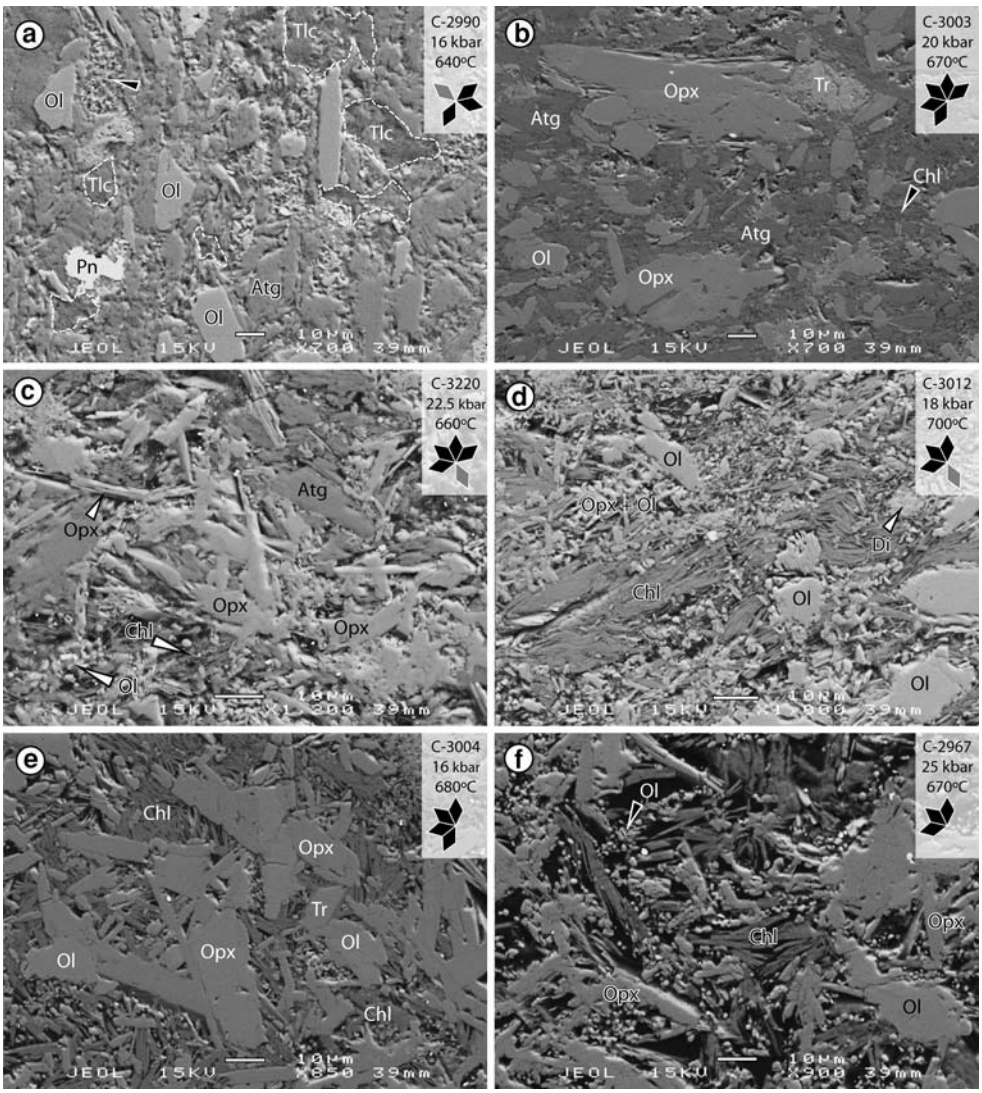

Fig. 5 Back-scatter electron images showing representative textures and assemblages of runs products. *Scale bars* represent 10 μm **a** Antigorite, talc and tremolite (not seen) coexist at 640°C and 1.6 GPa, olivine is relic from the starting material. Relics of added wollastonite forms porous aggregates intermixed with tremolite (*arrow*) **b** Texture after the talc breakdown and ol-in reaction where antigorite is stable with large prismatic orthopyroxene, anhedral olivine grains (>10 μm) and minor chlorite. **c** Same as **b** but with orthopyroxene needle crystals and small idiomorphic olivine grains (<5 μm). Chlorite flakes are interstitial and diopside occurs as irregular aggregates. **d** Texture after the antigorite breakdown. Chlorite is the only phase in the matrix where small idiomorphic olivine and orthopyroxene nucleate. Large olivine overgrowths occur on olivine seeds from the starting material. **e** Large olivine and prismatic orthopyroxene (>30 μm) growth in chlorite matrix. Tremolite is stable. **f** Elongated orthopyroxene and two olivine generations (small grain-sized and large overgrowths) are in equilibrium with chlorite in a highly porous texture

observed (C-3044, C-3003 and C-3220). These reactions were easily detected by SEM observations because of the growth of large euhedral orthopyroxene and minor olivine. There is a remarkable change in texture beyond the Tlc-out and Ol-in reactions where the assemblage Opx + Atg + Ol + Chl + Tr/Di is stable (compare Fig. 5a with Fig. 5b, c). The modal amount of olivine is lower than that of orthopyroxene. Olivine overgrowths relict grains from the starting material or occurs as small grain-sized euhedral crystals (usually 2–5 μm, Fig. 5c). Widespread needles of prismatic orthopyroxene (up to 30 μm in length) with nice crystal shapes grow in a matrix of antigorite and minor chlorite (Fig. 5b, c). The size of such needles is considerably larger than in the finely ground starting material, providing additional evidence for growth of orthopyroxene. Moreover, their aspect ratio is also high (3.1 ± 1.3, Fig. 5e). From thermodynamic analysis (Fig. 2, reaction 2), the Tlc-out curve must occur at lower temperatures than the Ol-in, reaction, although this could not be experimentally resolved with the temperature resolution used in the experiments. Tlc-out, Ol-in and Atg-out reactions converge at 1.5 GPa and 650–670°C (Fig. 4).

Atg-out reaction

At temperatures higher than 670–680°C, the disappearance of antigorite is easily detected by the increase of the modal amount of small olivine crystals (usually 2–4 μm), abundant orthopyroxene needles and chlorite flakes in the matrix (Fig. 5d–f). Moreover, water released from the complete antigorite dehydration (c. 8 wt% for this bulk composition) is evidenced by the high porosity developed in the resulting assemblage Ol + Opx + Chl + Tr/Di (e.g. Fig. 5f) and by the loss of weight of the experimental capsule after its piercing and drying in the oven (Table 2). Newly formed orthopyroxene and olivine are commonly free of inclusions (Fig. 5e). The antigorite-out reaction has a small pressure dependency in the pressure range investigated (1.6–2.5 GPa) increasing from 670°C and 1.6 GPa to 680°C at 1.9 GPa. At higher pressure (>1.9 GPa), it slightly bends back (c. 665°C at 2.5 GPa; Fig. 4).

Tr-out reaction

Tremolite is euhedral even at low temperatures. Nevertheless, the reactions involving tremolite and diopside are more sluggish compared with those involving antigorite owing to the different amount of water released. Newly formed diopside shows evidence of textural (Fig. 5d) and chemical disequilibrium (see below). In addition, very porous aggregates of relic wollastonite (added to the bulk composition) intermixed with diopside/tremolite (hard to analyse due to the small grain size) were common in some of the investigated runs (e.g. Fig. 5a). Therefore, the lack of tremolite was used to constrain the tremolite out curve (Fig. 4) instead of the appearance of diopside. With increasing temperature at pressures higher than 1.9-GPa tremolite disappears before the dehydration of antigorite. The Tr-out curves below and above the Atg-out curve (Fig. 4) correspond to reactions (7) and (8), respectively (Fig. 2).

Phase composition

Average major-element compositions of all phases analysed by EDS–SEM are available through electronic supplementary material (Supplementary Table).

Olivine

The main range of Fo-content [expressed as X_{Mg} = Mg/(Mg + Fe + Ni + Mn), in atoms] is 0.879–0.891 matching the range observed in olivine from the starting material (Table 1). No compositional variation among olivines in the various textures was observed. Also no systematic increase in X_{Mg} with temperature is present.

Antigorite

At temperatures higher than the Ol-in and Tlc-out curves antigorite is stable with chlorite and has a mean Al-content slightly lower than in the starting material (3.40–3.63 wt% Al_2O_3; Supplementary Table). At lower temperatures the amount of chlorite is minor or lacking, so the Al-content in antigorite is not buffered by the assemblage. The highest value (3.75 ± 0.33 wt% Al_2O_3) was found at 640°C and 1.6 GPa where no evidence of reaction was observed. The Cr_2O_3 content is also high (0.51–0.67 wt%) and similar to that of the starting material.

Chlorite and orthopyroxene

Chlorite displays a variation in aluminium with pressure. This variation can be explained through a series of substitutions: $^{IV}Al^{VI}AlSi_{-1}Mg_{-1}$ (tschermaks exchange), $^{IV}AlCr^{3+}Si_{-1}Mg_{-1}$ (Cr-tschermaks exchange) and, to a lesser extent, $^{IV}Al_2Ti^{4+}Si_{-2}Mg_{-1}$ (Ti-tschermaks exchange). Chromium content is high (1–2 wt% Cr_2O_3). A correlation between ^{IV}Al and $^{VI}Al + 2 \times Ti + Cr$ exists and is fairly dependent on pressure (Fig. 6a).

Orthopyroxene in the starting material, as well as in the low temperature assemblages, is almost aluminium-free (Table 1; Supplementary Table), whereas orthopyroxene in equilibrium with chlorite displays a significant increase in aluminium (0.45–1.13 wt% Al_2O_3). Similar to chlorite, orthopyroxene displays a good correlation of tetrahedral- and octahedral-coordinated aluminium. Tschermaks exchange in the orthopyroxene strongly increases with increasing pressure (Fig. 6b).

Other phases

Talc analyses show little chemical variation (Supplementary Table). Talc is low in Fe and Al and has a narrow X_{Mg} ratio of 0.972–0.977. No significant tschermaks substitution has been detected in tremolite with Al_2O_3 content within the range of the starting material (0.21 ± 0.12 wt%). Porous aggregates of diopside (Fig. 3f) were hard to analyse with systematic low totals and a wide range in X_{Mg} = 0.786–0.857 (Supplementary Table). Pentlandite is ubiquitous and occurs in all runs, whereas magnetite is lacking in some of them (Table 2). Magnetite is also chromium rich like in the starting material.

Mg partitioning

The order of preference for Mg expressed as X_{Mg} in the experiments is: talc > tremolite > chlorite > antigorite > orthopyroxene (Fig. 7). The observed sequence of Mg-partitioning between olivine and other phases is similar to

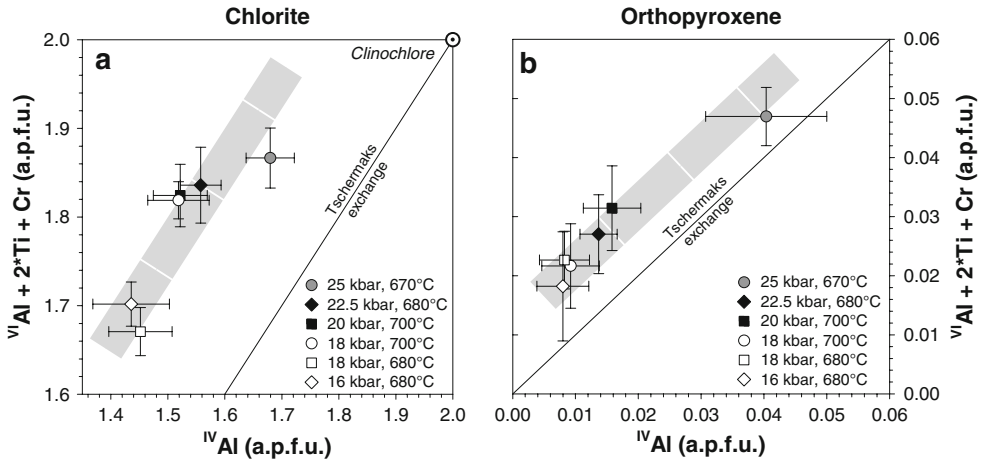

Fig. 6 Composition in atoms per formula unit (apfu) of experimentally determined chlorite and orthopyroxene in equilibrium with olivine. *Black* and *white symbols* represent high (>18 kbar) and low pressure runs (≤18 kbar), respectively. Run C-2967 performed on bulk-2 is indicated with *grey symbol*. **a** The tschermaks content in chlorite (normalised on 28 oxygens) increases with pressure but never reaches the clinochlore end-member in the PT range investigated. All analyses plot above the tschermaks exchange line indicating some extent of vacancies in the octahedral site. **b** Orthopyroxene (normalised to six oxygens) follows the same pattern. *Error bars* in **a** and **b** refer to 1σ errors of typically ≥5 analyses per run

those reported for other lower-P prograde serpentinite (Trommsdorff and Evans 1972, 1974; Springer 1974; Frost 1975) and high-P prograde serpentinite (Trommsdorff et al. 1998). One exception is diopside, not shown in Fig. 7, with a range in X_{Mg} of 0.786–0.857, far from the expected (X_{Mg} = 0.965–0.975) as observed in natural assemblages (cf. Trommsdorff and Evans 1972). Orthopyroxene also deviates slightly from the $K_d = 1.0$ line when chlorite is present at the highest temperature range investigated (670–700°C) reaching a maximum value of 0.909 ± 0.004 for a 0.886 ± 0.008 olivine (700°C and 2.0 GPa, run C-3011).

Discussion

Attainment of equilibrium

In the experiments reported here, the higher temperature runs show well-equilibrated textures where prismatic orthopyroxene and idiomorphic olivine grow in a chlorite matrix. (Fig. 5d–f). Moreover, the assemblage orthopyroxene–antigorite–olivine (Fig. 5b) is also texturally well equilibrated reproducing nicely the observed texture in the natural rocks (Fig. 3). However, lower temperature runs preserve olivine relics from the starting material suggesting only a partial equilibrium. Nevertheless, because the starting material contained minerals on the reactant and product side, reactions could be traced by the new growth and disappearance of phases. Additionally, the comparison of size and shape of minerals in the starting material with run products provides information on mineral growth. One interesting aspect of our study is that the appearance of a

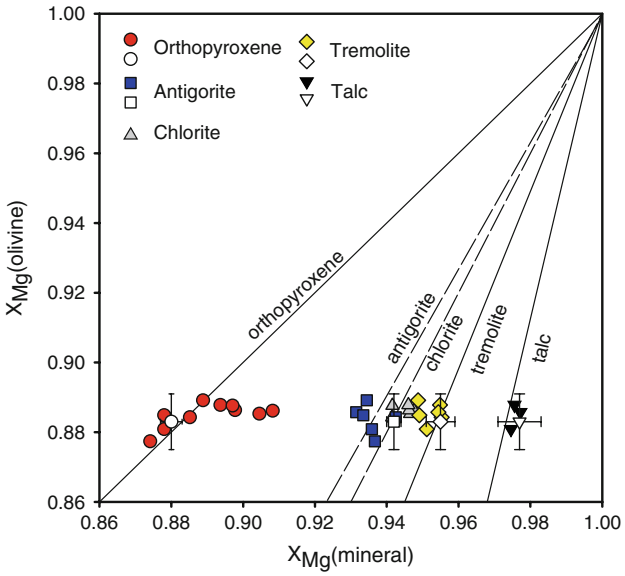

Fig. 7 Partitioning of Mg between olivine and other silicates [X_{Mg} is Mg atoms/(Mg + Fe + Mn + Ni) atoms]. *Solid lines* are taken from Trommsdorff and Evans (1972) except for chlorite and antigorite which are eye-ball fits. *Empty symbols with error bars* indicate the composition of the starting material showed in Table 1

new product phase (for example Opx) does not coincide with the complete disappearance of a reactant phase (for example talc). This could be interpreted at first sight as a "sluggish reaction." Instead, as shown in the next section, this is a direct consequence of the studied natural system, where reactions are continuous rather than discontinuous. The calculated temperature range of 20°C of fields between orthopyroxene-in and talc-out as well as olivine-in and antigorite-out (Fig. 8) is in very good agreement with the

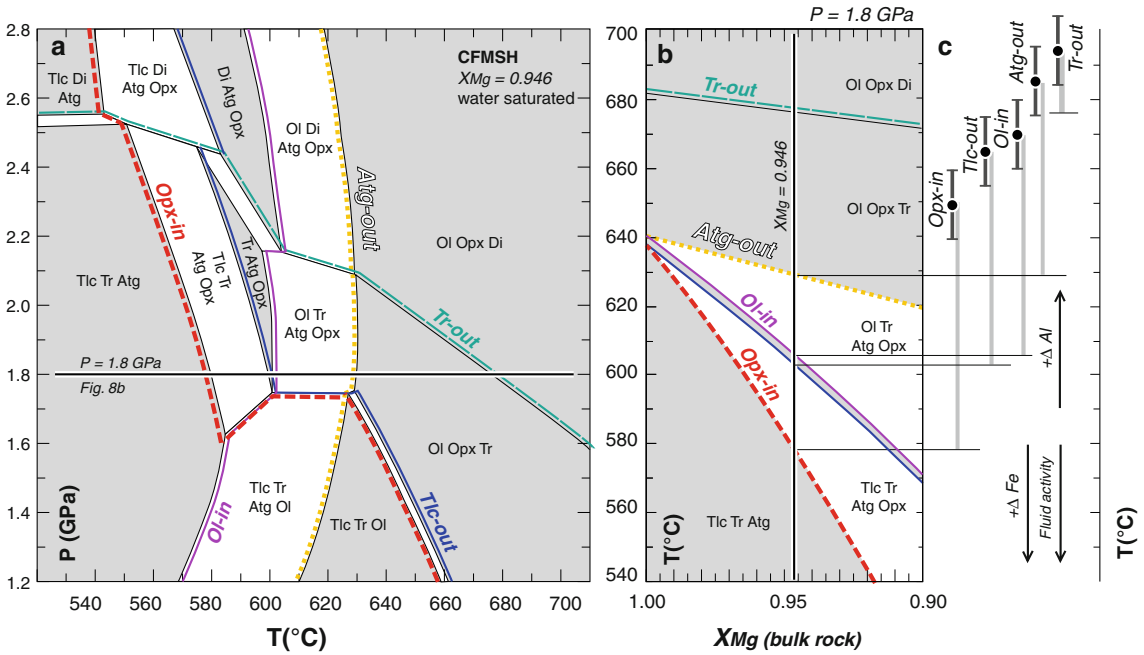

Fig. 8 **a** Pressure–temperature phase diagram section for a Si-enriched bulk composition (Al06-37, Table 1, bulk-3) in the CFMSH system computed with PerpleX (Connolly 2005). Solid solutions considered here are the same as in López Sánchez-Vizcaíno et al. 2005 (see their Table 6 for details). Thermodynamic data were taken from the internally consisted database of Holland and Powell (1998, revised 2002), except for the antigorite bulk modulus (Hilairet et al. 2006a). *White and grey fields* are divariant and trivariant fields, respectively. Lines dividing fields with the same variance are univariant reactions. Key reactions discussed in the text are labelled and highlighted with *different line symbols* (e.g. *red dashed line* for Opx-in) **b** Isobaric ($P = 1.8$ GPa) X_{Mg}-temperature pseudosection showing the temperature dependency of the fields from **a**. *Vertical line is the* X_{Mg} in Al06-37. **c** Temperature differences (*grey vertical lines*) between the experimentally determined (Fig. 4) and the computed curves of **b**. Temperature accuracy of thermocouples are depicted as *thick black brackets* (temperature gradient in the capsule and temperature hysteresis of the reactions are not considered here). These differences are attributed to aluminium in antigorite. The effect of iron and decrease of the fluid activity are also schematically showed with *arrows*

experimental data (Fig. 4). This suggests that no significant overstepping (not more than 10°C) is required for a reaction to progress.

Except for diopside, the order of Mg-partitioning in the experiments (Fig. 7) is the same as that observed in equivalent natural assemblages, indicating attainment of local chemical equilibrium. Also, there is no evidence for Fe-loss to the gold capsule. Departure from the equilibrium in the Mg partitioning may occur if the oxygen conditions change owing to hydrogen diffusion to the gold capsule. However, the presence of magnetite in equilibrium with the assemblage in most of the runs and the systematic occurrence of pentlandite point to constant oxygen and sulphur fugacity in the pressure and temperature range investigated. The magnesium enrichment in the orthopyroxene is most likely due to the tschermaks exchange ($Fe_{-1}Si^{VI}_{-1}Al^{IV}Al$) in equilibrium with chlorite. Indeed, if tschermaks is subtracted from the orthopyroxene composition, its X_{Mg} shifts to values closer to those of olivine (e.g. 0.898 ± 0.005 in C-3011). All these observations, suggest that the experiments partially approached equilibrium during the relatively long run durations.

Variables controlling the position of the antigorite dehydration

The antigorite composition in natural systems is complex and thus there are several variables influencing the position of the antigorite breakdown reaction (e.g. Ulmer and Trommsdorff 1999 and references therein). The effect of these additional components in antigorite must be evaluated before the experimental results from simplified systems can be applied to nature.

Iron is a major component that must be considered in natural serpentinite. A significant part of the iron in serpentinite occurs as magnetite as a result of complex reactions during the onset of serpentinization (e.g. Bach et al. 2006; Evans 2008; and reference therein) that increase the X_{Mg} in the minerals relative to their protolith. The role of magnetite during the antigorite dehydration has not yet been addressed but it is believed to behave as a passive phase. Moreover, magnetite occurs independently of the assemblage stable in the PT range investigated here (Table 2). The iron addition to the CMSH system can be evaluated by computing a fixed bulk composition, phase diagram section

("pseudosection"). Phase relations for the Si-enriched serpentinite bulk composition used in the experiments (bulk-3 in Table 1) were computed using Perple_X software (Connolly 2005) in the CFMSH system under water saturated conditions (Fig. 8a). Ferric iron content (see the analytical techniques section) was subtracted from the bulk composition resulting in a $X_{Mg} = 0.946$ [$X_{Mg} = Mg/(Mg + Fe)$, in molar proportion]. Considering that all ferric iron is forming magnetite the bulk composition would shift to a higher magnesium number ($X_{Mg} = 0.965$). Nevertheless the value of $X_{Mg} = 0.946$ was preferred because of the low modal amount of magnetite in Al06-37 (<3 vol%) supporting that most of the ferric iron from the bulk rock is hosted in antigorite.

Comparing the CMSH phase diagram (Fig. 2a) with the pseudosection computation (Fig. 8a) three main differences stand out: (1) the univariant reactions are now divariant fields in the CFMSH system; (2) invariant points are now transformed into univariant reactions, and (3) the terminal reactions (e.g. Atg-out) are displaced to lower temperatures relative to the CMSH system. The magnitude of the displacement and the extent of the divariant fields are directly related with the Fe–Mg partitioning of the different phases (Fig. 7). For instance, the iron effect on the extent of the divariant field equivalent to reaction (4) (Ol + Tlc = Opx + L, Fig. 2) is very minor (<5°C) in the CFMSH pseudosection (Fig. 8), because olivine and orthopyroxene (with a $K_D^{Mg-Fe} \sim 1.0$) occur on both sides of the reaction and because the talc composition is close to the Mg-endmember. This is not the case for the divariant fields equivalent to reactions (1) (Ol–Di–Atg–Opx field) and (2) (Tlc–Tr–Atg–Opx) in the CFMSH system, resulting in a considerable enlargement of the divariant fields and displacement of reactions to lower temperatures. The width of the divariant fields equivalent to reaction (1) and (2) is c. 20°C and c. 30°C at 1.8 GPa, respectively (Fig. 8a, b). Therefore, these fields can be detected with the experimental resolution used in this work. From the experimental results we conclude that the Opx-in and Tlc-out curves, as well as the Ol-in and Atg-out curves, are not coincident (Fig. 4). The temperature interval between the appearance and disappearance of these phases as calculated in the pseudosection is in good agreement with those experimentally observed (Fig. 8a).

The dependency of the antigorite breakdown reaction with decreasing bulk X_{Mg} can be inspected at a constant pressure in Fig. 8b. The position of the antigorite dehydration curve for $X_{Mg} = 0.946$ in the bulk rock (Atg-out in Fig. 8b) shrinks only 10°C relative to that of the CMSH system. The effect of bulk rock X_{Mg} is, however, much more pronounced for the appearance of orthopyroxene, which appears at 60°C lower than in the pure CMSH system (Fig. 8b).

Other components that must be addressed are aluminium and other trivalent cations like Fe^{3+} and Cr^{3+}. The pseudosection approach cannot be used in this case because there are no thermodynamic solid solution models for these cations in antigorite. Their effect in the terminal reactions can be, however, qualitatively assessed by comparing the positions of the experimentally determined curves (Fig. 4) with those calculated in the CFMSH system (Fig. 8b, c). The discrepancies in temperature between the calculated and observed curves are c. 60–70°C at 1.8 GPa. We interpreted these differences as due to the incorporation of Al and minor Cr and Fe^{3+} in the antigorite structure. Bromiley and Pawley (2003) reported a temperature difference between the antigorite dehydration curve in the MSH and MASH systems of about 50°C below 2.5 GPa, in good agreement with our results. Interestingly, the experimentally determined Tr-out curve almost matches that calculated in the pseudosection (Fig. 8b, c), because of the low Al solubility in clinopyroxene and tremolite for this pressure–temperature range.

The water activity of the fluid is also an important variable controlling the position of the antigorite dehydration equilibria in a P–T phase diagram. Although unknown, the water activity in our experimental runs is constrained by the assemblage and thus should correspond closely to that occurring in the nature. Lowering the water activity shifts the reaction to lower temperatures. Perrillat et al. (2005) reported a decrease of the water activity ($aH_2O = 0.5–0.8$) during experimental dehydration of Al-bearing antigorite at very low temperatures (570°C at 1.8 GPa). The lower water activity in their experiment was imposed by the type of containers (hexagonal boron nitride) required for the time-resolve X-ray diffraction measurement (Perrillat et al. 2005). Such a great reduction of water activity is unlikely to occur in nature. The composition of the fluid released during the antigorite dehydration is difficult to be constrained from fluid inclusions studies because fluid compositions are re-equilibrated with their host minerals (Scambelluri et al. 2001). At 750°C and 3.0 GPa antigorite dehydration fluids dissolve c. 6 wt% SiO_2, c. 2 wt% MgO and only minor amounts of CaO and Al_2O_3 (Tenthorey and Hermann 2004), and are thus essentially aqueous fluids.

Comparison to other studies

Since the pioneering work of Bowen and Tuttle (1949), the phase relations involving serpentine minerals (antigorite, crysotile and lizardite) have been intensively surveyed from the experimental point of view (Bromiley and Pawley 2003; Ulmer and Trommsdorff 1999 and references therein). Excluding studies at very high pressures (>5 GPa) (Bose and Navrotsky 1998), antigorite breakdown through

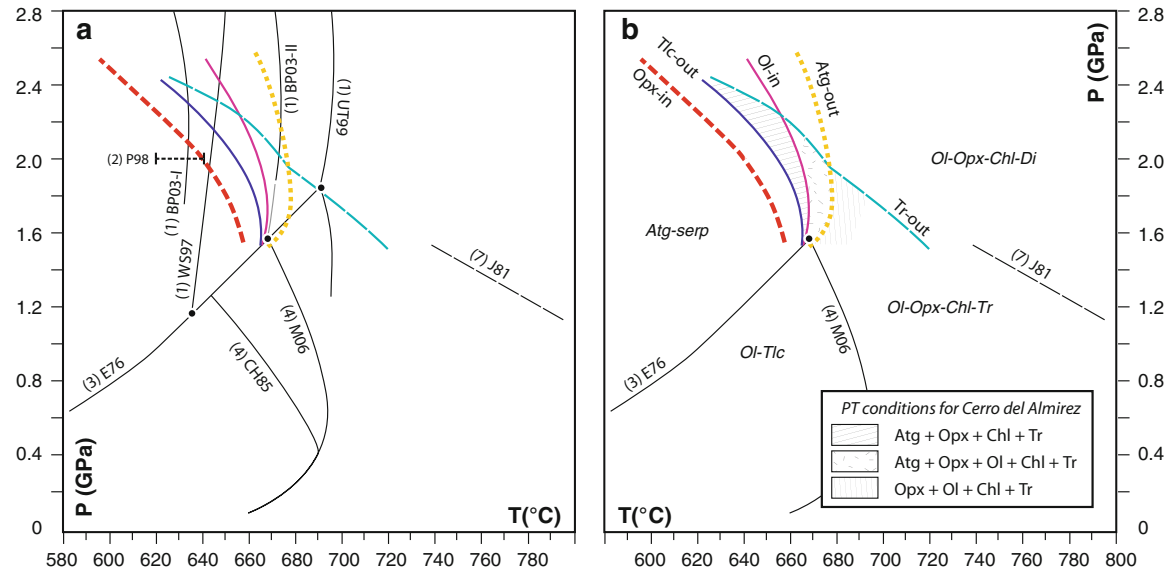

Fig. 9 **a** Summary of selected experimental curves involving the antigorite breakdown. The *numbers in brackets* indicate the reactions as showed in Fig. 2. Experimental fits are by E76—Evans et al. (1976); J81—Jenkins (1981); CH85—Chernosky et al. (1985); WS97—Wunder and Schreyer (1997); UT99—Ulmer and Trommsdorff (1999); BP03-I and BP03-II- Bromiley and Pawley (2003) for free-Al (0.01 wt% Al_2O_3) and Al-bearing antigorite (3.06 wt% Al_2O_3), respectively; M06—Melekhova et al. (2006). The bracket of reaction (2) P98 from Pawley (1998) is also showed. Superimposed are the experimentally determined *curves* from this study (curve patterns as in Figs 8, 9b). Also shown are the invariant points [Di] (*filled black dots*) at the intersection of reaction (3) E76 and reactions (1) and (4) from previous works. **b** Preferred experimentally-based petrogenetic grid for Si-enriched bulk composition from Cerro del Almirez. PT-conditions inferred for the antigorite + orthopyroxene + chlorite + tremolite assemblage, antigorite + orthopyroxene + olivine + chlorite + tremolite and olivine + orthopyroxene + chlorite + tremolite assemblage (prograde harzburgite) in Cerro del Almirez are depicted with different patterns

reaction (1) (antigorite = forsterite + orthopyroxene + water) has been bracketed by many authors (Ulmer and Trommsdorff 1995; Wunder and Schreyer 1997; Bromiley and Pawley 2003; Komabayashi et al. 2005), and, at lower pressure, through reaction (4) (antigorite = forsterite + talc + water) by Johannes (1975) and Evans et al. (1976).

The iron effect on the position of the antigorite dehydration curve is minor, as discussed before, but has to be taken into account when comparing the results obtained here with previous works. Although all the previous experimental studies were addressed to establish the antigorite stability in the MSH or MASH systems, they used natural antigorite that invariably contained appreciable amounts of FeO (specially in the case of Ulmer and Trommsdorff 1995 and sample BM1913,87 from Bromiley and Pawley 2003).

Figure 9a and b shows the positions of the antigorite terminal reaction as determined in the present study compared to previous work. Ulmer and Trommsdorff (1999) reported higher temperature stability for antigorite (~20°C) compared to the antigorite breakdown reaction observed here (Atg-out, Fig. 9). The same reaction, when reported by Wunder and Schreyer (1997), occurs at c. 40°C lower temperatures. The significant discrepancy between the position of reaction (1) by Ulmer and Trommsdorff (1995) and Wunder and Schreyer (1997) has been already discussed by Wunder and Schreyer (1997), Mysen et al. (1998) and Bromiley and Pawley (2003). They concluded that the most likely explanation is the contrasting Al-content of the antigorite used in these studies and, to a lesser extent, other trivalent cations such as Cr^{3+} and Fe^{3+}. However, in this discrepancy the higher Fe-content of the natural antigorite (with a $X_{Mg} = 0.965$) used by Ulmer and Trommsdorff (1995) compared to the almost Fe-free antigorite ($X_{Mg} = 0.991$) from Wunder and Schreyer (1997) must also be taken into account. The X_{Mg} of our starting material is similar to the X_{Mg} of the natural antigorite from sample Mg159 chosen by Ulmer and Trommsdorff (1999), but their sample contains less trivalent cations (Mellini et al. 1987). Thus, the reason for the higher temperature of antigorite breakdown reported by Ulmer and Trommsdorff (1999) is not fully clear. We expect that the antigorite-out reaction determined here is located close to the maximum temperature for natural systems as the antigorite from our study has the highest Al-content among all experimental studies.

Bromiley and Pawley (2003) conducted a series of experiments of antigorite dehydration in the MSH and (F)MASH systems in order to demonstrate the stabilisation of antigorite to considerably higher temperatures and

pressures in the presence of Al. They found that at 2 GPa the antigorite stability field expands by c. 40°C from about 630°C for Al-free antigorite to 670°C for Al-bearing antigorite (3.06 wt% Al_2O_3) [curves (1)BP03-I and (1)BP03-II, respectively in Fig. 9a]. At higher pressure the thermal difference is even larger (90°C at 5 GPa). The Al-bearing antigorite dehydration curve experimentally determined by Bromiley and Pawley (2003) is in excellent agreement with the results presented here for an antigorite with 3.70 wt% Al_2O_3 and 0.59 wt% Cr_2O_3. Moreover, their natural antigorite BM1913,87 ($X_{Mg} = 0.916$) and the antigorite used in this study ($X_{Mg} = 0.942$) share a relatively high iron content. Therefore, it is expected that the Al-effect would be even greater (>40°C) for Fe-poor antigorite. The antigorite used in the starting material for this study contains high amounts of aluminium and chromium and derives from rocks that were formed in a high pressure environment. Hence, the experimentally determined breakdown of antigorite reported here should closely match the one expected in natural subducted serpentinites between 1.6 and 2.5 GPa.

In silica-rich bulk compositions (Fig. 1), a first antigorite dehydration reaction (2) occurs at considerably lower temperature (Fig. 2). This reaction has only been experimentally investigated by Pawley (1998) in the MSH system. She determined the position of the reaction at 2 GPa to be situated between 620 and 640°C [bracket (2) P98 in Fig. 9a], which is in agreement with our results for the Opx-in curve (Fig. 9a, b). The invariant point [Di] in MSH (Fig. 2a) arises at the intersection of reactions (1) and (2). Considering the divariant fields, this corresponds with a narrow temperature range of 660–670°C at c. 1.6 GPa, where all the terminal reactions corresponding with reactions (1) and (2) converge (Fig. 4). This is in good agreement with the intersection of reaction (1) from Bromiley and Pawley (2003), reaction (3) (Atg = Ol + Tlc + L) from Evans et al. (1976) and reaction (4) (Ol + Tlc = Opx + L) from Melekhova et al. (2006) at 670°C and 1.6 GPa (Fig. 9a, b). Reaction (4) is independent of the antigorite Al-content and rather insensitive to the Fe-effect and thus can be used independently to constrain the position of the invariant point [Di]. Reaction (4) (Melekhova et al. 2006) intersects with the Atg-out curve from this study and from Bromiley and Pawley (2003) in their (F)MASH system at about 1.6 GPa. As outlined in the previous section, the invariant point [Di] in MSH will translate into a univariant line in FMSH (Fig. 8a) that terminates the Atg + Opx assemblage at 1.8 GPa. Due to the negative slope of the reaction (4), the termination of Atg + Opx will be displaced to lower pressure of 1.6 GPa and slightly higher temperature with the increasing of Al-content in the antigorite.

The tremolite-out reactions [reactions (7) and (8)] have been poorly constrained experimentally. Jenkins (1981) reported experiments up to 1.4 GPa in the CMASH system of the reaction (7) (Tr + Ol = Di + Opx). The slope of this reaction is in agreement with the results reported here (Fig. 4). It is worth noting that the reaction (6) could not be determined using the starting material of this study but its intersection with reaction (1) must occur at 680°C and 1.9 GPa at the invariant point [Tlc] in the CMSH system (Fig. 2).

PT conditions of Cerro del Almirez

The experimental approach used here permits to constrain the pressure and temperature conditions for the Ol + Opx + Chl + Tr assemblage (termed chlorite harzburgite by Garrido et al. 2005) extensively outcropping in Cerro del Almirez, as well as for the Atg + Opx + Ol + Tr assemblage outcropping only as metre-sized lenses close to the antigorite isograd. The antigorite stability field found in this study constrains the minimum temperature for the chlorite harzburgite between 660 and 680°C at temperatures between 1.6 and 2.5 GPa, (Fig. 9b). The occurrence of tremolite in the Ol + Opx + Chl rocks limits the pressure below 1.9 GPa. The Tr-out reaction also constrains the maximum temperature, which ranges from 680 to 710°C for 1.9 and 1.6 GPa, respectively.

The PT conditions for the antigorite dehydration in Cerro del Almirez has been previously constrained (1.7–2.0 GPa and 635–640°C) combining thermodynamic modeling (pseudosections) of selected Cerro del Almirez bulk composition (López Sánchez-Vizcaíno et al. 2005, 2009) with the PT conditions for the equilibrium between OH-titanclinohumite and ilmenite + olivine fitting the experimentally determined reaction by Weiss (1997) (see also Ulmer and Trommsdorff 1999). López Sánchez-Vizcaíno et al. (2005) estimated a minimum temperature of about 650°C for the prograde assemblage at P = 1.70–2.05 GPa. The uncertainty on the FeO/Fe_2O_3 ratio was overcome by subtracting different modal amounts of magnetite occurring in the Almirez serpentinites (López Sánchez-Vizcaíno et al. 2005). The thermodynamic data for the antigorite iron endmember was taken from Rupke et al. (2004) and an ideal mixing model was considered. The large aluminium content in the Cerro del Almirez antigorite (up to 4 wt% Al_2O_3, Trommsdorff et al. 1998; Padrón-Navarta et al. 2008) is a common feature of serpentinites from high-grade terranes (Uehara and Kamata 1994; Auzende et al. 2002, 2006). However a solution model for Al in the antigorite is not yet available. Moreover, a new experimentally determined equation of state for the antigorite indicates that the isothermal bulk modulus (K_0) was underestimated in the Holland and Powell's (1998) database. The updated bulk

modulus shrinks the stability of the antigorite to lower temperature and pressures (c. 10°C at 1.8 GPa, Hilairet et al. 2006a, 2006b; Nestola, personal communication, 2009). The lack of a solid solution model for a chlorite-component in antigorite and the underestimated bulk modulus for the antigorite in the thermodynamic dataset (Holland and Powell 1998, revised 2002) used by López Sánchez-Vizcaíno et al. (2005) explain the slightly lower temperatures previously reported for the minimum temperature for the chlorite harzburgite.

The pressure conditions for the chlorite harzburgite reported here are consistent with those estimated for the metamorphic peak in the upper series of the Nevado–Filábride complex. Puga et al. (1999, 2002) found a temperature range from 650 to 725°C at 1.8 GPa using the Grt–Cpx geothermometer of Ellis and Green (1979) in eclogitized dykes preserved in metarodingites from the Cerro Blanco-Montenegro outcrop (20 km eastwards from Cerro del Almirez), in agreement with our results. However, their pressure constraints are based on the experimental curves from Ulmer and Trommsdorff (1995) and Wunder and Schreyer (1997) and, as discussed before, cannot be directly applied to the Cerro del Almirez. Eclogites studied in other areas of the Nevado–Filábride complex indicated pressures of 1.2–1.3 GPa and 500–540°C (Gómez-Pugnaire and Fernández-Soler 1987) and near 1.5 GPa and 700°C (Puga et al. 1989). Other lithologies (scapolite-bearing metaevaporites) point to a minimum pressure of 1.8 GPa at 500–650°C (Gómez-Pugnaire et al. 1994). The maximum pressure recorded in the metapelites from the upper series are deduced by the assemblage of chloritoid + staurolite + almandine + kyanite, suggesting pressure values of 1.5–1.7 GPa for 600°C (Puga et al. 2002). In any case the chlorite harzburgite from Cerro del Almirez preserves the highest temperatures recorded by the Nevado–Filábride complex rocks.

New antigorite dehydration in silica enriched serpentinite

The present study constrains the pressure-temperature conditions for the assemblage Atg + Opx and Atg + Opx + Ol in equilibrium with tremolite and minor chlorite under water saturated conditions (Fig. 9b). Opx-bearing serpentinite with or without olivine is stable between 640 and 680°C and pressure higher than 1.6 GPa. The bulk chemistry of these rocks indicates an enrichment of silica relative to other common serpentinites (Fig. 1). The resulting assemblage is diagnostic of metaperidotites that experienced silica metasomatism (Manning 1994, 1995, 2004; Peacock and Hyndman 1999). Si-rich serpentinite may be a common lithology in mid-ocean ridge and subduction settings.

At the basement of slow-spreading mid-ocean ridges, peridotite is heavily veined, with talc and talc-oxide-sulphide veins (Bach et al. 2006). Earlier serpentinized peridotite undergoes massive replacement by talc, forming amphibole-chlorite-talc schists (Bach et al. 2004). These metasomatic reactions require either removal of Mg or addition of Si to the system. In the mid-Atlantic ridge, talc-altered rocks are formed by silica metasomatism, where silica is mobilised from gabbros and harzburgite undergoing high-temperature (>350°C) fluid–rock interactions (Bach et al. 2006; Paulick et al. 2006; Alt et al. 2007). Seawater-alteration coupled with Mg-removal generates serpentinites with anomalously high SiO_2/MgO ratios, which are reported in ophiolites (Marchesi et al. 2006) and abyssal peridotites (Snow and Dick 1995). Hence, Si-rich serpentinites produced either by Si-metasomatism or Mg loss during mid-ocean ridge processes may be a common input in subduction zones.

Antigorite-talc schist may also form during prograde metamorphism in subduction settings as a result of chaotically intermixing of ultramafic rocks with metasediments and metabasites in a mélange zone (Moore and Lockner 2007; King et al. 2003; King and Bebout 2006; Spandler et al. 2008). Si-enriched ultramafic rocks such as talc-schist and talc-bearing serpentinite have been observed in several HP rock suites (Sorensen and Grossman 1989, 1993; Bebout and Barton 2002; Spandler et al. 2008). These hybrid rocks are interpreted as the result of the interaction of ultramafic rocks with Si-rich fluid (Spandler et al. 2008). Si-rich fluids can be provided by the dehydration of mafic and metasedimentary rocks in the blueschist/eclogite-facies transition (Clarke et al. 1997; Spandler et al. 2003, 2008) and hence it is expected that Si-enriched ultramafic rocks are common in the serpentinized mantle wedge above subduction zones.

Talc-schist and talc-bearing serpentinite may hence be common lithologies in subduction settings and will undergo different dehydration reactions. Antigorite and talc will react at lower temperature than the terminal antigorite dehydration. Although this reaction is not expected to be as important in the transfer of water to mantle depth as the breakdown of antigorite, it represents nevertheless a dehydration event in subduction zones that has not been considered so far. We anticipate that this reaction might be particularly important for the fore-arc mantle wedge. The amount of water released would depend on the modal proportion of these two phases that is ultimately related with the degree of interaction of the ultramafic rocks with the metasomatic fluid. The appearance of orthopyroxene in talc-bearing serpentinite is restricted to pressures higher than 1.6 GPa inside the antigorite stability field. Moreover, the transition from tremolite to diopside at 2.3–2.5 GPa is an additional excellent barometer in silica enriched

serpentinites (Figs. 2, 8). The Opx-serpentinite facies is thus helpful in the reconstruction of PT conditions of subducted ultramafic rocks where common serpentinites have no diagnostic assemblage over a large range in PT space (Scambelluri et al. 1995; Hermann et al. 2000).

Conclusions

Piston cylinder experiments on silica enriched serpentinites from the Cerro del Almirez ultramafic complex constrain the maximum temperature stability for highly polysomatic ordered ($m = 15$–16) antigorite with high-Al and Cr contents to 680°C at 1.9 GPa. This is also the maximum pressure stability of tremolite in an olivine + orthopyroxene + chlorite assemblage. In this bulk composition, the olivine-in reaction occurs 20–30°C below the antigorite-out reaction. At 1.8 GPa, Al and other trivalent cations in antigorite expand its stability 60–70°C when compared with the Al-free system. The maximum temperature for antigorite stability is bracketed between 680 and 660°C at 1.6 and 2.5 GPa. The Tr-out reaction also constrains the maximum temperature for chlorite harzburgite from Cerro del Almirez, which ranges from 680 to 710°C for 1.9 and 1.6 GPa. These data are in reasonable agreement with peak P–T conditions estimated for the Nevado–Filabride complex upper series. Orthopyroxene + antigorite assemblage is restricted to high-pressure metamorphic conditions of silica enriched serpentinite, and constraints P–T conditions in cold to intermediate temperature subduction environments, where antigorite serpentinite has no diagnostic assemblages over a large pressure and temperature range.

In silica enriched serpentinites, antigorite and talc dehydrate at lower temperature than the final breakdown of antigorite. This dehydration reaction releases a variable amount of water depending on the relative proportion of talc and antigorite, and represents therefore a lower temperature dehydration event in Si-metasomatized, subducted ultramafic rocks.

Acknowledgments Three anonymous reviewers are thanked for their insightful and helpful reviews. We thank D. Scott, W.O. Hibberson and D. Clark for their technical support in the running of the high-pressure experiments at the RSES (ANU) and Frank Brink for his technical assistance in the Electron Microscopy Unit (ANU). We also thank Prof. Marcello Mellini for his comments on an early draft of the paper. This work was supported by the Spanish "Ministerio de Ciencia e Innovación (MICINN)" through research grants CGL2006-04440, CGL2007-61205/BTE, and ACI2006-A9-0580, the Spanish Council for Research (CSIC) through grant 2008-30I014, and by the "Junta de Andalucía" research groups RNM-145 and RNM-131. J.A. Padrón-Navarta1 is supported by fellowship AP2005-060 from the "Programa de Formación del Profesorado Universitario". J. Hermann acknowledges financial support by the Australian Research Council. We are grateful for the editorial help and support provided by J. Hoefs.

References

Alt JC, Shanks WC, Bach W, Paulick H, Garrido CJ, Beaudoin G (2007) Hydrothermal alteration and microbial sulfate reduction in peridotite and gabbro exposed by detachment faulting at the Mid-Atlantic Ridge, 15°20′N (ODP Leg 209): a sulfur and oxygen isotope study. Geochem Geophys Geosyst 8:Q08002. doi:10.1029/2007GC001617

Arai S (1975) Contact metamorphosed dunite–harzburgite complex in the Chugoku district, western Japan. Contrib Mineral Petrol 52:1–16

Auzende AL, Devouard B, Guillot S, Daniel I, Baronnet A, Lardeaux JM (2002) Serpentinites from Central Cuba: petrology and HRTEM study. Eur J Mineral 14:905–914

Auzende A-L, Guillot S, Devouard B, Baronnet A (2006) Serpentinites in an Alpine convergent setting: effects of metamorphic grade and deformation on microstructures. Eur J Mineral 18:21–33

Bach W, Garrido CJ, Paulick H, Harvey J, Rosner M (2004) Seawater–peridotite interactions: first insights from ODP Leg 209, MAR 15°N. Geochem Geophys Geosyst 5:Q09F26. doi: 10.1029/2004GC000744

Bach W, Paulick H, Garrido CJ, Ildefonse B, Meurer WP, Humphris SE (2006) Unraveling the sequence of serpentinization reactions: petrography, mineral chemistry, and petrophysics of serpentinites from MAR 15°N (ODP Leg 209, Site 1274). Geophys Res Lett 33(13):L13306. doi:10.1029/2006GL025681

Bebout GE, Barton MD (1989) Fluid-flow and metasomatism in a subduction zone hydrothermal system—Catalina-Schist Terrane, California. Geology 17:976–980

Bebout GE, Barton MD (2002) Tectonic and metasomatic mixing in a high-T, subduction-zone mélange-insights into the geochemical evolution of the slab–mantle interface. Chem Geol 187:79–106

Boillot G, Feraud G, Recq M, Girardeau J (1989) Undercrusting by serpentinite beneath rifted margins. Nature 341:523–525

Bose K, Navrotsky A (1998) Thermochemistry and phase equilibria of hydrous phases in the system $MgO–SiO_2–H_2O$: implications for volatile transport to the mantle. J Geophys Res Solid Earth 103:9713–9719

Bowen NL, Tuttle OF (1949) The system $MgO–SiO_2–H_2O$. Geol Soc Am Bull 60:439–460

Bromiley GD, Pawley AR (2003) The stability of antigorite in the systems $MgO–SiO_2–H_2O$ (MSH) and $MgO–Al_2O_3–SiO_2–H_2O$ (MASH): the effects of Al^{3+} substitution on high-pressure stability. Am Mineral 88:99–108

Capitani G, Mellini M (2004) The modulated crystal structure of antigorite: the $m = 17$ polysome. Am Mineral 89:147–158

Chernosky JV, Day HW, Caruso LJ (1985) Equilibria in the system $MgO–SiO_2–H_2O$—experimental-determination of the stability of Mg-anthophyllite. Am Mineral 70:223–236

Clarke GL, Aitchison JC, Cluzel D (1997) Eclogites and blueschists of the Pam Peninsula, NE New Caledonia: a reappraisal. J Petrol 38:843–876

Connolly JAD (2005) Computation of phase equilibria by linear programming: a tool for geodynamic modeling and its application to subduction zone decarbonation. Earth Planet Sci Lett 236:524–541

Ellis DJ, Green DH (1979) An experimental study of the effect of Ca upon garnet-clinopyroxene Fe–Mg exchange equilibria. Contrib Mineral Petrol 71:13–22

Evans BW (1977) Metamorphism of Alpine peridotite and serpentinite. Annu Rev Earth Planet Sci 5:397–447

Evans BW (2008) Control of the products of serpentinization by the $Fe^{2+}Mg_{-1}$ exchange potential of olivine and orthopyroxene. J Petrol 49(10):1873–1887. doi:10.1093/petrology/egn050

Evans BW, Johannes W, Oterdoom H, Trommsdorff V (1976) Stability of crysotile and serpentinite in the serpentine multisystem. Schweiz Mineral Petrogr Mitt 56:79–93

Frost R (1975) Contact metamorphism of serpentinite, chloritic blackwall and rodingite at Paddy-Go-Easy Pass, Central Cascades, Washington. J Petrol 16:272–313

Fumagalli P, Poli S (2005) Experimentally determined phase relations in hydrous peridotites to 6.5 GPa and their consequences on the dynamics of subduction zones. J Petrol 46:555–578

Garrido CJ, López Sánchez-Vizcaíno V, Gómez-Pugnaire MT, Trommsdorff V, Alard O, Bodinier JL, Godard M (2005) Enrichment of HFSE in chlorite-harzburgite produced by high-pressure dehydration of antigorite–serpentinite: implications for subduction magmatism. Geochem Geophys Geosyst 6:Q01J15. doi:10.1029/2004GC000791

Gómez-Pugnaire MT, Fernández-Soler JM (1987) High-pressure metamorphism in metabasites from the Betic Cordilleras (S.E. Spain) and its evolution during the Alpine orogeny. Contrib Mineral Petrol 95:231–244

Gómez-Pugnaire MT, Franz G, López Sánchez-Vizcaíno V (1994) Retrograde formation of NaCl-scapolite in high pressure metaevaporites from the Cordilleras Béticas (Spain). Contrib Mineral Petrol 116:448–461

Guillot S, Hattori KH, de Sigoyer J (2000) Mantle wedge serpentinization and exhumation of eclogites: insights from eastern Ladakh, northwest Himalaya. Geology 28:199–202

Guillot S, Hattori KH, de Sigoyer J, Nagler T, Auzende AL (2001) Evidence of hydration of the mantle wedge and its role in the exhumation of eclogites. Earth Planet Sci Lett 193:115–127

Hermann J, Spandler CJ (2008) Sediment melts at sub-arc depths: an experimental study. J Petrol 49:717–740

Hermann J, Müntener O, Scambelluri M (2000) The importance of serpentinite mylonites for subduction and exhumation of oceanic crust. Tectonophysics 327:225–238

Hilairet N, Daniel I, Reynard B (2006a) Equation of state of antigorite, stability field of serpentines, and seismicity in subduction zones. Geophys Res Lett 33:L02302. doi:10.1029/2005GL024728

Hilairet N, Daniel I, Reynard B (2006b) P–V equations of state and the relative stabilities of serpentine varieties. Phys Chem Miner 33:629–637

Holland TJB, Powell R (1998) An internally consistent thermodynamic data set for phases of petrological interest. J Metamorph Geol 16:309–343

Irving AJ, Ashley PM (1976) Amphibole-olivine-spinel, cordierite-anthophyllite and related hornfelses associated with metamorphosed serpentinites in the goobarragandra district, near Tumut, New South Wales. Aust J Earth Sci 23:19–43

Iwamori H, Zhao DP (2000) Melting and seismic structure beneath the northeast Japan arc. Geophys Res Lett 27:425–428

Jenkins DM (1981) Experimental phase relations of hydrous peridotites modelled in the system H_2O–CaO–MgO–Al_2O_3–SiO_2. Contrib Mineral Petrol 77:166–176

Johannes W (1975) Zur synthese and thermischen stabilität von antigorite. Fortschr Mineral 53:36

Kawakatsu H, Watada S (2007) Seismic evidence for deep-water transportation in the mantle. Science 316:1468–1471

King RL, Bebout GE (2006) Metamorphic evolution along the slab/mantle interface within subduction zones. Geochim Cosmochim Acta 70:A319–A319

King RL, Kohn MJ, Eiler JM (2003) Constraints on the petrologic structure of the subduction zone slab-mantle interface from Franciscan Complex exotic ultramafic blocks. Geol Soc Am Bull 115:1097–1109

Komabayashi T, Hirose K, Funakoshi K-i, Takafuji N (2005) Stability of phase A in antigorite (serpentine) composition determined by in situ X-ray pressure observations. Phys Earth Planet Inter 151(3–4):276–289

Lagabrielle Y, Bodinier J-L (2008) Submarine reworking of exhumed subcontinental mantle rocks: field evidence from the Lherz peridotites, French Pyrenees. Terra Nova 20:11–21

López Sánchez-Vizcaíno V, Rubatto D, Gómez-Pugnaire MT, Trommsdorff V, Müntener O (2001) Middle Miocene high-pressure metamorphism and fast exhumation of the Nevado–Filabride Complex, SE Spain. Terra Nova 13:327–332

López Sánchez-Vizcaíno V, Trommsdorff V, Gómez-Pugnaire MT, Garrido CJ, Müntener O, Connolly JAD (2005) Petrology of titanian clinohumite and olivine at the high-pressure breakdown of antigorite serpentinite to chlorite harzburgite (Almirez Massif, S. Spain). Contrib Mineral Petrol 149:627–646

López Sánchez-Vizcaíno V, Gómez-Pugnaire MT, Garrido CJ, Padrón-Navarta JA, Mellini M (2009) Breakdown mechanisms of titanclinohumite in antigorite serpentinite (Cerro del Almirez massif, S. Spain): a petrological and TEM study. Lithos 107(3–4):216–226. doi:10.1016/j.lithos.2008.10.008

Manning CE (1994) The solubility of quartz in H_2O in the lower crust and upper mantle. Geochim Cosmochim Acta 58:4831–4839

Manning CE (1995) Phase–equilibrium controls on SiO_2: metasomatism by aqueous fluid in subduction zones: reaction at constant pressure and temperature. Int Geol Rev 37:1074–1093

Manning CE (2004) The chemistry of subduction-zone fluids. Earth Planet Sci Lett 223:1–16

Marchesi C, Garrido CJ, Godard M, Proenza JA, Gervilla F, Blanco-Moreno J (2006) Petrogenesis of highly depleted peridotites and gabbroic rocks from the Mayari-Baracoa Ophiolitic Belt (eastern Cuba). Contrib Mineral Petrol 151(6):717–736. doi:710.1007/s00410-00006-00089-00410

Matthes S, Knauer E (1981) The phase petrology of the contact metamorphic serpentinite nera Erbendorf, Oberpfalz, Bavaria. Neues Jahrb Geol Palaontol Abh 141:59–89

Melekhova E, Schmidt MW, Ulmer P, Guggenbühl E (2006) The reaction talc plus forsterite = enstatite plus H_2O revisited: application of conventional and novel experimental techniques and derivation of revised thermodynamic properties. Am Mineral 91:1081–1088

Mellini M, Trommsdorff V, Compagnoni R (1987) Antigorite polysomatism—behavior during progressive metamorphism. Contrib Mineral Petrol 97:147–155

Moore D, Lockner D (2007) Comparative deformation behavior of minerals in serpentinized ultramafic rock: application to the slab–mantle interface in subduction zones. Int Geol Rev 49:401–415

Mysen BO, Ulmer P, Konzett J, Schmidt MW (1998) The upper mantle near convergent plate boundaries. In: Hemley RJ (ed) Ultrahigh-Pressure mineralogy: physics and chemistry of the Earth's deep interior, vol 37. Mineralogical Society of America, Washington, pp 97–138

Nozaka T, Shibata T (1995) Mineral paragenesis in thermally metamorphosed serpentinites, Ohsa-yama, Okayama Prefecture. Okayama Univ Earth Sci Rep 2(1):1–11

O'Hanley D (1996) Serpentinites: records of petrologic and tectonic history. Oxford University Press, Oxford, p 277

Padrón-Navarta JA, López Sánchez-Vizcaíno V, Garrido CJ, Gómez-Pugnaire MT, Jabaloy A, Capitani G, Mellini M (2008) Highly ordered antigorite from Cerro del Almirez HP–HT serpentinites, SE Spain. Contrib Mineral Petrol 156:679–688

Paulick H, Bach W, Godard M, De Hoog JCM, Suhr G, Harvey J (2006) Geochemistry of abyssal peridotites (Mid-Atlantic Ridge, 15°20'N, ODP Leg 209): implications for fluid/rock interaction in slow spreading environments. Chem Geol 234:179–210

Pawley AR (1998) The reaction talc plus forsterite = enstatite plus H_2O: new experimental results and petrological implication. Am Mineral 83:51–57

Peacock SM (2001) Are the lower planes of double seismic zones caused by serpentine dehydration in subducting oceanic mantle? Geology 29:299–302

Peacock SM, Hyndman RD (1999) Hydrous minerals in the mantle wedge and the maximum depth of subduction thrust earthquakes. Geophys Res Lett 26:2517–2520

Perrillat JP, Daniel I, Koga KT, Reynard B, Cardon H, Crichton WA (2005) Kinetics of antigorite dehydration: a real-time X-ray diffraction study. Earth Planet Sci Lett 236:899–913

Pickering JM, Schwab BE, Johnston AD (1998) Off-center hot spots: double thermocouple determination of the thermal gradient in a 1.27-cm (1/2in) CaF2 piston-cylinder furnace assembly. Am Mineral 83:228–235

Pinsent RH, Hirst DM (1977) The metamorphism of the Blue River ultramafic body, Cassiar, British Columbia, Canada. J Petrol 18:567–594

Puga E, Díaz de Federico A, Fediukova E, Bondi M, Morten L (1989) Petrology, geochemistry and metamorphic evolution of the ophiolitic eclogites and related rocks from the Sierra Nevada (Betic Cordilleras, Southeastern Spain). Schweiz Mineral Petrogr Mitt 69:435–455

Puga E, Nieto JM, Díaz de Federico A, Bodinier JL, Morten L (1999) Petrology and metamorphic evolution of ultramafic rocks and dolerite dykes of the Betic Ophiolitic Association (Mulhacen Complex, SE Spain): evidence of eo-Alpine subduction following an ocean-floor metasomatic process. Lithos 49:23–56

Puga E, Díaz de Federico A, Nieto JM (2002) Tectonostratigraphic subdivision and petrological characterisation of the deepest complexes of the Betic zone: a review. Geodinamica Acta 15:23–43

Ranero CR, Morgan JP, McIntosh K, Reichert C (2003) Bending-related faulting and mantle serpentinization at the Middle America trench. Nature 425:367–373

Rupke LH, Morgan JP, Hort M, Connolly JAD (2004) Serpentine and the subduction zone water cycle. Earth Planet Sci Lett 223:17–34

Scambelluri M, Müntener O, Hermann J, Piccardo GB, Trommsdorff V (1995) Subduction of water into the mantle—history of an alpine peridotite. Geology 23:459–462

Scambelluri M, Bottazzi P, Trommsdorff V, Vannucci R, Hermann J, Gómez-Pugnaire MT, López Sánchez-Vizcaíno V (2001) Incompatible element-rich fluids released by antigorite breakdown in deeply subducted mantle. Earth Planet Sci Lett 192:457–470

Scambelluri M, Fiebig J, Malaspina N, Müntener O, Pettke T (2004a) Serpentinite subduction: implications for fluid processes and trace-element recycling. Int Geol Rev 46:595–613

Scambelluri M, Müntener O, Ottolini L, Pettke TT, Vannucci R (2004b) The fate of B, Cl and Li in the subducted oceanic mantle and in the antigorite breakdown fluids. Earth Planet Sci Lett 222:217–234

Scambelluri M, Malaspina N, Hermann J (2007) Subduction fluids and their interaction with the mantle wedge: a perspective from the study of high-pressure ultramafic rocks. Period Mineral 76:253–265

Schilling F, Wunder B (2004) Temperature distribution in piston-cylinder assemblies: numerical simulations and laboratory experiments. Eur J Mineral 16:7–14

Schmidt MW, Poli S (1998) Experimentally based water budgets for dehydrating slabs and consequences for arc magma generation. Earth Planet Sci Lett 163:361–379

Snow JE, Dick HJB (1995) Pervasive magnesium loss by marine weathering of peridotite. Geochim Cosmochim Acta 59(20):4219–4235

Sorensen SS, Grossman JN (1989) Enrichment of trace elements in garnet amphibolites from a paleo-subduction zone: Catalina Schist, southern California. Geochim Cosmochim Acta 53:3155–3177

Sorensen SS, Grossman JN (1993) Accessory minerals and subduction zone metasomatism—a geochemical comparison of 2 melanges (Washington and California, USA). Chem Geol 110:269–297

Spandler C, Hermann J, Arculus R, Mavrogenes J (2003) Redistribution of trace elements during prograde metamorphism from lawsonite blueschist to eclogite facies; implications for deep subduction-zone processes. Contrib Mineral Petrol 146:205–222

Spandler C, Hermann J, Faure K, Mavrogenes J, Arculus R (2008) The importance of talc and chlorite "hybrid" rocks for volatile recycling through subduction zones; evidence from the high-pressure subduction mélange of New Caledonia. Contrib Mineral Petrol 155:181–198

Springer RK (1974) Contact Metamorphosed Ultramafic Rocks in the Western Sierra Nevada Foothills, California. J Petrol 15:160–195

Tatsumi Y (1989) Migration of fluid phases and genesis of basalt magmas in subduction zones. J Geophys Res Solid Earth Planets 94:4697–4707

Tenthorey E, Hermann J (2004) Composition of fluids during serpentinite breakdown in subduction zones: evidence for limited boron mobility. Geology 32:865–868

Torres-Roldán RL, García-Casco A, García-Sanchez PA (2000) CSpace: an integrated workplace for the graphical and algebraic analysis of phase assemblages on 32-bit wintel platforms. Comput Geosci 26:779–793

Trommsdorff V, Evans BW (1972) Progressive metamorphism of antigorite schist in the Bergell tonalite aureole (Italy). Am J Sci 272:423–437

Trommsdorff V, Evans BW (1974) Alpine metamorphism of peridotitic rocks. Schweiz Mineral Petrogr Mitt 72:229–242

Trommsdorff V, López Sánchez-Vizcaíno V, Gómez-Pugnaire MT, Müntener O (1998) High pressure breakdown of antigorite to spinifex-textured olivine and orthopyroxene, SE Spain. Contrib Mineral Petrol 132:139–148

Uehara S, Kamata K (1994) Antigorite with a large supercell from Saganoseki, Oita prefecture, Japan. Can Mineral 32:93–103

Ulmer P, Trommsdorff V (1995) Serpentine stability to mantle depths and subduction-related magmatism. Science 268:858–861

Ulmer P, Trommsdorff V (1999) Phase relations of hydrous mantle subducting to 300 km. In: Fei Y, Bertka CM, Mysen BO (eds) Mantle petrology: field observations and high pressure experimentation. Special Publication No. 6. The Geochemical Society, Houston, pp 259–281

Vance JA, Dungan MA (1977) Formation of peridotites by deserpentinization in the Darrington and Sultan areas, Cascade Mountains, Washington. Geol Soc Am Bull 88:1497–1508

Watson E, Wark D, Price J, Van Orman J (2002) Mapping the thermal structure of solid-media pressure assemblies. Contrib Mineral Petrol 142:640–652

Weiss M (1997) Clinohumites: a field and experimental study. Ph.D. thesis. ETH, Zurich, p 168

Worden RH, Droop GTR, Champness PE (1991) The reaction antigorite = olivine + talc + H_2O in the Bergell aureole, N. Italy. Mineral Mag 55:367–377

Wunder B, Schreyer W (1997) Antigorite: high-pressure stability in the system MgO–SiO_2–H_2O (MSH). Lithos 41:213–227

Wunder B, Wirth R, Gottschalk M (2001) Antigorite: pressure and temperature dependence of polysomatism and water content. Eur J Mineral 13:485–495